Thin–Walled Structures 210 (2025) 113048

Contents lists available at ScienceDirect

Thin-Walled Structures

journal homepage: www.elsevier.com/locate/tws

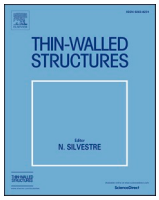

Novel test designs for assessing the shear fracture forming limit in thin-walled tubes

C. Suntaxi [a], J.A. López-Fernández [b], G. Centeno [c,*], C. Vallellano [c]

[a] Departamento de Ingeniería Mecánica, Facultad de Ingeniería Mecánica, Escuela Politécnica Nacional, Quito, Ecuador
[b] Department of Civil, Materials and Manufacturing Engineering, University of Málaga, Málaga, Spain
[c] Department of Mechanical and Manufacturing Engineering, University of Seville, Sevilla, Spain

ARTICLE INFO

Keywords:
Shear fracture forming limit (SFFL)
Forming limit diagram (FLD)
Thin-walled tube, Shear
Fracture

ABSTRACT

Thin-walled tubes are used for the manufacturing of essential components in several industries. Indeed, the characterization of their formability and failure is vital for tool design, product quality and safety. In the recent years, the number of procedures and test designs for characterizing tubes in forming has experienced a significant development. This progress has been achieved in combination with the use of digital image correlation techniques and finite element analysis, making use of different plastic anisotropy criteria. Nevertheless, most of those tests are aimed at the assessment of failure in mode I of fracture mechanics, being the analysis of fracture under in-plane shear, i.e. mode II of fracture mechanics, reduced to a very limited number of research works based in the adaptation of the corresponding sheet metal forming tests inducing shear. To this regard, this work presents two new procedures based on the specific thin-walled tube geometry for characterizing formability in-plane shear and failure in mode II of fracture mechanics, addressing the absence of specific experimental methods for evaluating the shear fracture forming limit (SFFL) for tubes. The results, based on a combined numerical modelling and experimental analysis of the proposed tests, show that the SFFL can be accurately evaluated by controlling a set of geometrical parameters in the specimens designed to generate shear in tubes by applying either tensile or compressive forces. These proposed tests provide a valuable tool for characterizing the SFFL of thin-walled tubes.

1. Introduction

A thin-walled tube is a hollow cylindrical structure with a relatively small wall thickness compared to its outer diameter. In other words, the wall of a thin-walled tube is thin in relation to its overall size, allowing to provide, due to its particular geometry, a high strength to weight ratio. Industrial tubes are typically made from various materials such as metals (e.g., steel, aluminium, titanium), plastics, or composites [1]. The key defining characteristic of a thin-walled tube is thus its high ratio of diameter to wall thickness, which makes it structurally different from thicker-walled pipes or solid cylinders.

Thin-walled tubes are known for their lightweight and efficient use of material, and are consequently widely used in various industries, including aerospace [2,3], automotive [4,5] and construction [6–8], as well as other applications where weight reduction, efficient material utilization and structural integrity are important considerations. Tubes can be easily shaped, bent, welded, or manipulated to suit specific engineering needs, making them versatile components in many engineering and manufacturing processes.

To this regard, the characterization of the forming limits of a material is critical for understanding the stress/strain states upon which it can be plastically deformed. Concerning sheet metal, the establishment of a framework for the analysis of these forming limits began with the work by Keeler [9] and Goodwin [10] by the late 60′s of the 20th century. Those investigations supposed the origin of circle grid analysis (CGA) techniques and are considered as the basis of current Forming Limit Diagrams or FLD's.

In this sense, Embury and Duncan [11] were pioneer in the use of the principal strain space for the characterization of failure by fracture, associating fracture in mode I of fracture mechanics (in-plane tension) to a failure locus with a slope of "−1″ within this strain space, thus coinciding with the condition of critical thickness reduction [12]. Indeed, the work on fracture in forming by Atkins [12] connected fracture in mode I, using stress triaxiality, with the McClintock fracture criterion

* Corresponding author.
E-mail address: gaceba@us.es (G. Centeno).

https://doi.org/10.1016/j.tws.2025.113048
Received 4 July 2024; Received in revised form 5 December 2024; Accepted 3 February 2025
Available online 6 February 2025

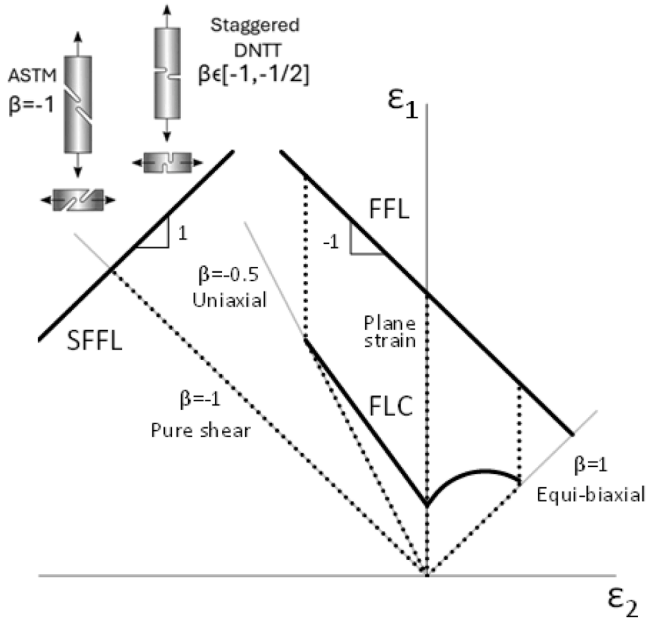

Fig. 1. Schematic representation of the FLD adapted from Martins et al. [16].

based on void growth [13].

More recently, the work by Silva et al. [14] provided a novel vision for the overall assessment of forming limits by fracture in sheet metal forming, including procedures and tests for the determination of the forming limit in mode I of fracture mechanics (in-plane tension), i.e. the fracture forming limit (FFL), but also in mode II (in-plane shear), i.e. the shear fracture forming limit (SFFL). On the other hand, the assessment of the onset of necking can be addressed by a series of procedures for the determination of the forming limit curve (FLC), as explained in detail in related research work as [15]. The overall schematic representation of the resulting forming limits within the FLD in sheet metal forming is provided in Fig. 1, adapted from Martins et al. [16], depicting test geometries that might excite in-plane shear in the case of sheet metal as well as in their adaptation to tubes both along the longitudinal and the circumferential directions. Other testing geometries exiting shear were also recently proposed by Mai et al. [17] for evaluating shear yielding and failure of cold-reduced steel sheets. This can be used in combination with theoretical and experimental approaches such as [18] for modelling ductile fracture of this kind of steel sheets, as well as other materials.

Concerning formability of thin-walled tubes, in the last decades a series of works have focussed on assessing their formability limits, most of them based on hydroforming [19], mainly aiming the characterization of the forming limit at the onset of necking, such as the works by Chen et al. [20] and Li et al. [21]. Nevertheless, some works [22,23] brought into light that, in certain cases, the strain attained in hydroforming could reach values above the material FLC, justifying the evaluation of the fracture forming limit or FFL in thin-walled tubes, as it is typically carried out in sheet metal [16].

In this scientific context, the authors initiated in 2016 [24] a research line towards the combined characterization of the forming limits at necking and fracture of thin-walled tubes. These research works included the analysis of tube edge expansions with conical [24] and shaped [25] punches, internal expansions [26] as well as tube inversions [27]. The overall assessment of the tube FLD, including FLC and FFL, allowed the evaluation of formability and fracture in non-proportional processes such as in SPIF of tubes [28], pointing out that the evolution of the average stress triaxiality [29] during the process evolves for values below 0.33 [30], which usually corresponds to in-plane shear. This fact, together with the possible interest in tube forming processes involving shear, make necessary the establishment of procedures for the assessment of the SFFL for tubes.

To this regard and as far as the authors are concerned, there are very few existing methodologies for assessing the SFFL for thin walled tubes [31], being the current state of the art limited to the adaptation of tensile specimens with notches using similar geometries to those utilized in sheet metal forming (as depicted in Fig. 1), such as those proposed by Shouler and Allwood [32], Kerim et al. [33] or Silva et al. [34]. In any case, the number of research works dedicated to the determination of the SFFL is very limited [31] and the tests are not always adapted to the specific tube geometry.

For all those reasons, this research is pioneering in presenting two new procedures specifically conceptualized assuming the tube geometry for characterizing mode II failure in thin-walled tubes using the well-known fundamentals of sheet metal forming. These proposed 2 tests, as well as their numerical models and experimental methods developed, addressed the above discussed lack of experimental procedures for evaluating the shear fracture forming limits (SFFL) of tubes. The results, based on a combined numerical modelling and experimental approach, show that the SFFL can be accurately evaluated by controlling a number of defined geometrical parameters in the testing specimens specifically designed to generate shear in thin-walled tubes by applying either tensile or compressive forces.

The results, which combine numerical and experimental approaches, demonstrate that the SFFL can be accurately assessed by applying either tensile or compressive forces on tubular specimens. This is achieved by systematically controlling specific geometric parameters in the specimens that induce shear in thin-walled tubes.

2. Design of in-plane shear tests for tubes

This section aims presenting the procedure followed for the design of the two novel shear tests for the assessment of the SFFL in thin-walled tubes. To this regard, Section 2.1 introduces the general procedure for the design of the two new tests, Section 2.2 focuses on the so-named shear test by compression (STC), whereas Section 2.3 corresponds to the design of the shear test by tension (STT).

The design of both shear tests is carried out considering a commercial AA6061-T4 thin-walled tube of 1.5 inches of average external diameter and 0.049 inches of average wall thickness, which is the actual tube material that is used later in the forming experiments.

2.1. Design of shear tests for tubes

Related to the design of suitable tests for tubes, it must be pointed out again that currently there is no standardized procedure for the assessment of the SFFL in tubes making use of the specific tube geometry. As a result, it is necessary the development of a comprehensive and universally accepted experimental testing framework that outlines this specific geometry, including the testing parameters that might be appropriate for the shear tube forming tests. This will ensure a more accurate and efficient evaluation of the SFFL, thus enhancing the reliability and effectiveness of the tests designed.

To this regard, the theoretical SFFL line [16] could be determined by the assessment of a fracture point (ε^{o}_{2f}, ε^{0}_{1f}) and imposing a slope with a value of 1. However, the theoretical value of the slope is not always close to 1, and thus the most adequate strategy is to determine experimentally a number of fracture points corresponding to a variety of principal strain paths defined by different values of the strain ratio $\beta = \varepsilon_2/\varepsilon_1$ in the range from uniaxial strain ($\beta = -1/2$) towards pure shear ($\beta = -1$).

With the aim of inducing a variety of strain ratios within the shear zone, a parametric study was utilized to generate a diversity of 3D geometries for both tests, which should induce different strain states and thus different strain ratios β, based on the selected geometric parameters. For this purpose, finite element (FE) simulations were used to evaluate the impact of the selected geometric parameters on the

resulting strain loading paths. Following this iterative numerical analysis, a limited number of specific values of the parameters were established in order to determine a range of strain loading paths for providing a number of fracture points used to assess a realistic SFFL.

In addition, the design process of the geometries producing shear required specific characteristics such as: symmetrical geometry to prevent bending, a deformation zone without local buckling, no more than three geometrical parameters, a gripping device that avoid unwanted deformations and, of course, a simple geometry that facilitate the manufacture of both of the test dies and the specimens. After evaluating a number of alternatives, two specimen geometries were identified for fulfilling those requirements. They are presented, described and numerically analysed in the following sections.

Finally, it must be pointed out that the selection of the process parameters is based on the dimensions of typical machining tools for the manufacturing of the testing specimens combined with a number of try and error preliminary simulations that aimed achieving the desired strain paths.

2.2. Shear test by compression (STC)

This section presents one of the two test designs developed for the assessment of the SFFL, in this case by using a novel specimen geometry and the corresponding forming die to be used with a testing setup under compressive forces. In the STC test design, depicted in Fig. 2a, the shear area is delimited by two slots, a horizontal slot with a given width defined as w and a diameter d, and a vertical slot with a width defined as a and a corner radius indicated as r_t. These slots are connected by the ligament with a value h. As can be seen in Fig. 2a, the compressive load F produces a shear force on the ligament that is applied through a protruding zone of the die.

In this sense, the selected parameters (r_t, w and h) for conducting the FE numerical simulations and their values are presented in Table 1, resulting in 36 possible combinations. To reduce this number of numerical simulations, the influence of each parameter on the strain path was assessed via an iterative procedure, discarding some sets of parameter values that produced undesired results. In addition, the values of a and d were set to 5 mm, aligning with the standard size of the cutting tool.

The numerical model for the compression shear test was carried out using the flow-deformation based finite elements software DEFORM-3D™, using symmetry conditions, as depicted in Fig. 2b. The bottom die (punch) is modelled as a non-deformable solid and moves upwards at a constant speed of 0.9 mm/s, whereas the top die (plate) is a non-deformable fixed element. A Tresca friction model $\tau = mk$ is assumed at the interfaces bottom die-testing specimen and top die-testing specimen, being k the shear yield stress and setting a value of $m = 0.05$ based on friction considerations from previous works [27,30]. The discretization of the model was performed using a mesh of 50,000 tetrahedrons of 1 mm size, with a finer mesh of 0.25 mm in the ligament region. The finite element analysis employed an isotropic elastoplastic material model and a Mises yield criterion.

Table 1
Selected values of the process parameters for the STC test.

r_t **(mm)**	2.5 / 1.5 / 0.1
w **(mm)**	5 / 7.5 / 10 / 12.5
h (mm)	3 / 5
a **(mm)**	5
d (mm)	5

The material properties and plastic flow curve for the 6061-T4 aluminium tube were obtained for this initial analysis from the DEFORM-3D library. Initially, as well as the precise instant at the onset of shear fracture is unknown, the simulation was stopped following a displacement criterion for the bottom die, defined for $\Delta y = 0.2h$. To this regard, it must be noticed that the main objective of this initial analysis is limited to obtain the strain paths provided by the different sets of parameters for their actual selection, but not for assessing each test until the instant of fracture. The precise value of Δy corresponding to failure is later updated in a second stage by making use of the experimental results. In the numerical analysis, the initiation point of fracture is assumed to be at the location where the shear stress is maximum. This criterion is also later refined by combining the experimental data with the numerical simulation.

The FE simulations are thus used to iteratively analyse the influence of the corner radius r_t, width w, and ligament size h, in that order. In the initial approximation, a ratio of $w/h = 1$ is fixed, resulting in an aspect ratio of 1:1 for the shear zone. The geometric parameters were modified

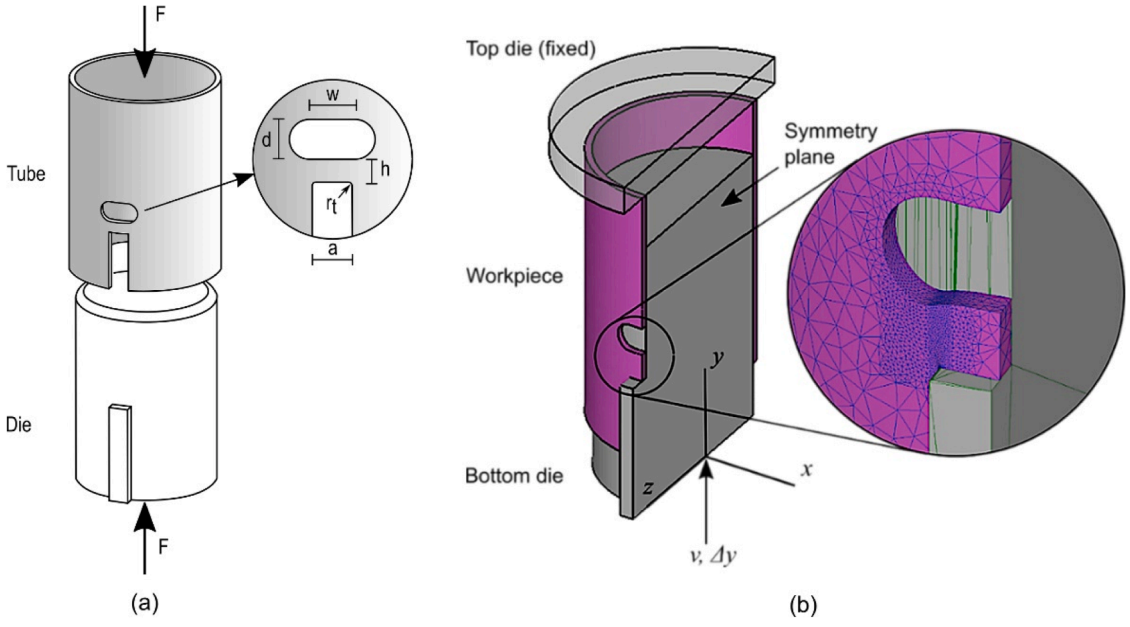

Fig. 2. (a) Schematic representation of the shear test by compression or STC and (b) numerical model of the STC (***w*** = 5 ***mm***, ***h*** = 5 ***mm***) carried out using DEFORM-3D™.

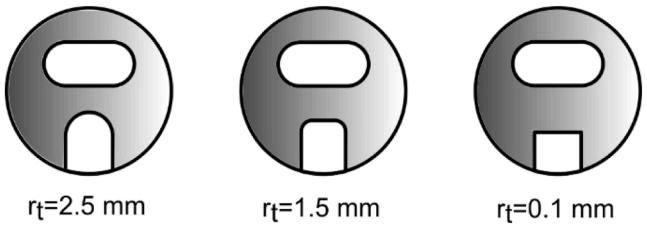

Fig. 3. Detail of shapes and dimensions of the notches for the STC ($\boldsymbol{w} = 5$ ***mm***, $\boldsymbol{d} = 5$ ***mm***).

using values of $r_t = \{2.5,\ 1.5,\ 0.1\}$ *mm*, which led to the formation of the notch shapes depicted in Fig. 3.

In the case of the radius $r_t = 2.5$ *mm*, the contact between the die and the ligament causes a compressive stress, resulting in an increase of thickness. This combination of compressive stresses leads to a strain path with $\beta < -1$. However, this effect can be mitigated by using a smaller corner radius. By employing corner radii of 1.5 mm and 0.1 mm, strain paths close to $\beta = -1$ can be achieved. Fig. 4 shows the strain loading paths for each radius r_t considered, with the 0.1 mm radius producing a more proportional and linear path. For the subsequent analysis, a value of $r_t = 0.1$ *mm* was set.

After setting $r_t = 0.1$ *mm*, the 4 values of width $w = \{5,\ 7.5,\ 10,\ 12.5\}$ *mm* were combined with 2 values of the height $h = \{3,\ 5\}$ *mm*. This generates the 8 strain loading paths shown in Fig. 4b. As can be seen, some strain loading paths are very close to each other and even overlap, as in the case of the 10×3 and 12.5×3 combinations.

Based on the results provided in Fig. 4, the four representative cases with regularly spaced strain loading paths depicted in Fig. 5 were finally selected. The corresponding set of parameters was used for manufacturing the actual specimens to be tested in the experimentation of the STC test.

2.3. Shear test by tension (STT)

The second design to characterize the SFFL makes use of another novel test specimen together with dedicated tools and testing setup to perform the experiments under tensile conditions. As shown in Fig. 6a, the STT specimen comprises a shearing area defined by two through drills of diameter *d*, forming the line connecting the centres of the drills an angle α relative to the longitudinal axis of the tube. Coupling

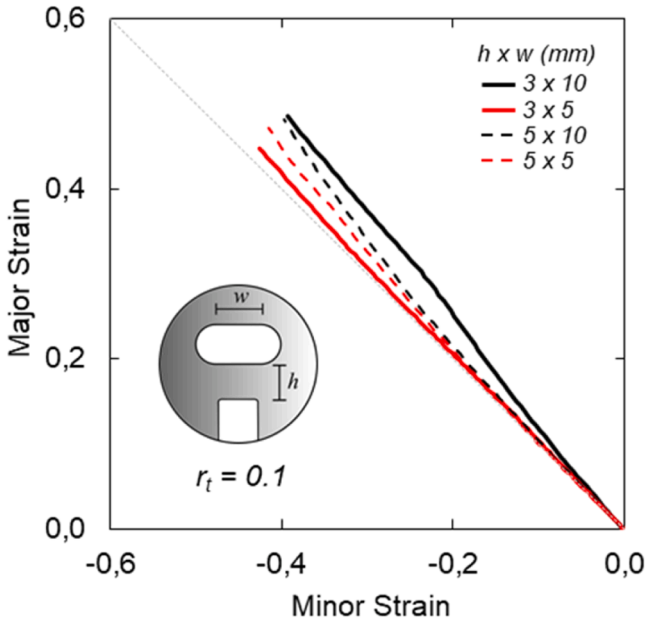

Fig. 5. Selected set of parameters and corresponding strain paths with $\boldsymbol{w} = \{5,\ 10\}$ ***mm*** and $\boldsymbol{h} = \{3,\ 5\}$ ***mm***.

elements, depicted as *clamping device* in Fig. 6b, secure the tube and allow applying a tension load *F*, resulting in shear stress at the ligament of height *h* between the centre of the drills.

Analogously to the case of the STC test, a series of parameters (i.e. *d*, h and α) and their values were selected (see Table 2) for conducting the numerical analysis based on FE, resulting again in 36 possible combinations. To reduce this number of combinations, the effect of each parameter on the strain path was assessed via a sequential procedure. In this sense, the numerically prediction first examined the effect of the hole diameter *d*, then the ligament size *h*, and finally the angle α on the strain loading path.

In this case, as shown in Fig. 6c a symmetry model of the STT test is carried out. This numerical model was performed using a mesh of 60,000 tetrahedrons with a finer mesh in the ligament region (shear zone). The clamping devices (top and bottom) are modelled as rigid bodies. The top die moves upwards at a constant velocity of $v =$

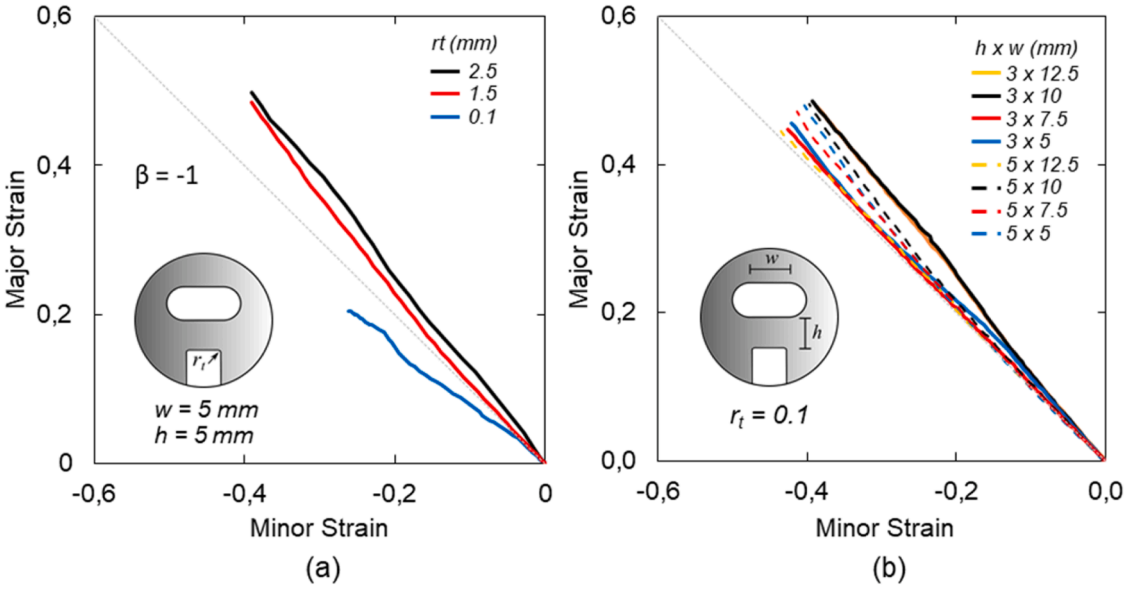

Fig. 4. Numerical strain loading paths for (a) $\boldsymbol{r_t} = \{2.5,\ 1.5,\ 0.1\}$ ***mm*** and (b) for $\boldsymbol{w} = \{5,\ 7.5,\ 10,\ 12,5\}$ ***mm*** and $\boldsymbol{h} = \{3,\ 5\}$ ***mm*** after setting $\boldsymbol{r_t} = 0.1$.

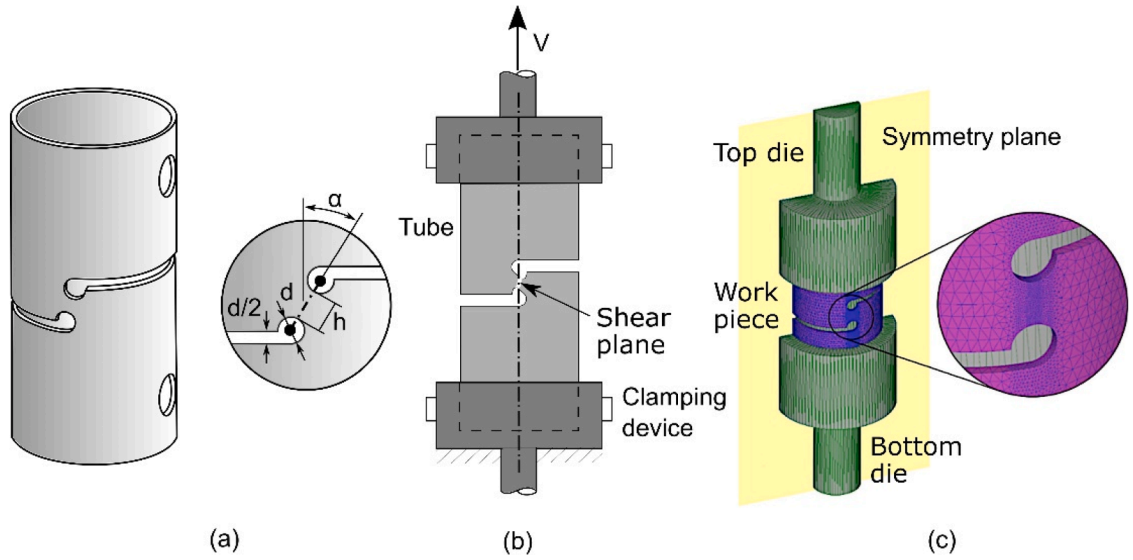

Fig. 6. (a) Schematic representation of the shear test by tension or STT, (b) front view indicating the shear zone and clamping device and (c) numerical model of the STT carried out using DEFORM-3D™.

Table 2
Selected values of the process parameters for the STT test.

d (mm)	5 / 4 / 3
h (mm)	5 / 4 / 3
α (mm)	−15° / 0° / 15° / 30°

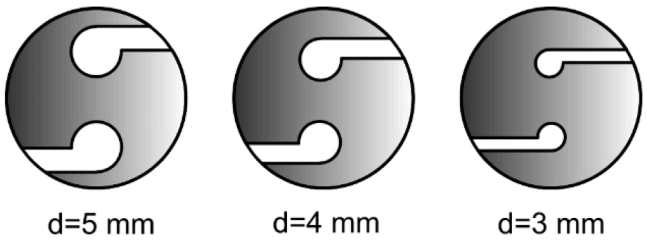

Fig. 7. Detail of shapes and dimensions of the shear zone for different hole diameters ($\boldsymbol{\alpha} = 0°$, $\boldsymbol{h} = 5$ $\boldsymbol{mm}$).

0.9 mm/s, whereas the bottom die remains fixed. In order to achieve higher accuracy, a gradual mesh refinement is applied in the shear zone. Again, a Tresca friction model with a value of $m = 0.05$ is set between the interfaces of the dies with the tube. As well as in the case of the STC test, an isotropic elastoplastic material with a Mises yield criterion is considered. The material properties for the 6061-T4 aluminium tube in this initial numerical analysis are taken from DEFORM-3D's library. The simulation is halted using a displacement criterion based on a reference point, estimated as $\Delta y = 0.8h$ based on preliminary experimental results.

As explained above, an analysis of the effects of drill hole size d, ligament size w, and orientation angle α was performed in this order to identify the most suitable values for these parameters. In this sense, Fig. 7 shows the tube shapes in the shear zone obtained by varying the hole diameter using values of $d = \{2.5,\ 1.5,\ 0.1\}$ mm, whereas the orientation angle α is set to 0° and the ligament size h to 5 mm.

As can be easily assumed from the results shown in Fig. 8a, the effect of the hole diameter d on the path loading strains is negligible. However, simulations using larger diameters have been performed concluding that it is not advisable the use of much larger diameters because failure could occur by crack opening in Mode I of fracture mechanics. Under these circumstances, a hole diameter of 5 mm was chosen in order to ease the specimens manufacturing, avoiding the use of very thin machining tools.

In the case of the ligament size h, its effect on the strain loading path was analysed by varying its dimensions of $h = \{5,\ 4,\ 3\}$ mm, as previously indicated in Table 2. The strain loading path resulted to be quite sensitive to the variation of the ligament size, as can be seen in Fig. 8b. Indeed, in the case of a 3 mm ligament, bending was found to be noticeably greater than shear, resulting in a strain ratio with a slope close to $\beta = -1/2$ that corresponds to uniaxial strain, indicating that fracture might occur in mode I. Ligament sizes of 4 mm and 5 mm produced similar results, being the latter value selected.

Finally, the analysis of the effect of the orientation angle α on the strain loading path was carried out varying the values of $\alpha = \{-15°,\ 0°,\ 15°,\ 30°\}$, maintaining constant the values of $d = 5$ mm and $h = 5$ mm. The results of the numerical predictions shown in Fig. 9 show that the strain loading path for an angle of 0° had a slope very close to $\beta = -1$ (pure shear). In the case of increasing the angle to 15°, the slope increased slightly, whereas for the case of the 30° angle of, the strain ratio was close to $\beta = -1/2$ (uniaxial strain), which would imply fracture in mode I. Using the negative angle of −15° had the same effect as the 30° angle, producing bending. Therefore, it was concluded that increasing the angle led to a combined mode between shear and uniaxial tension.

The overall numerical analysis conducted facilitated the identification of the sets of process parameter that made it feasible the establishment of a limited experimental plan for performing the tube shear test under tension or STT test. Together with the selected set of parameters for the STC test, the experimental plan for assessing the SFFL in tube is presented in the following section.

3. Experimentation

Section 3 presents the experimentation performed for assessing of the SFFL in thin-walled tubes: Section 3.1 concerning the tensile tests for the determination of the stress-strain curve in plastic regime, and Section 3.2 focusing on the shear test by compression (STC) and by tension (STT), including the experimental equipment utilised, the experimental plan, the strain measurement and the determination of failure strains.

3.1. Tensile tests

As explained in Section 2, the AA6061-T4 thin-walled tube used in

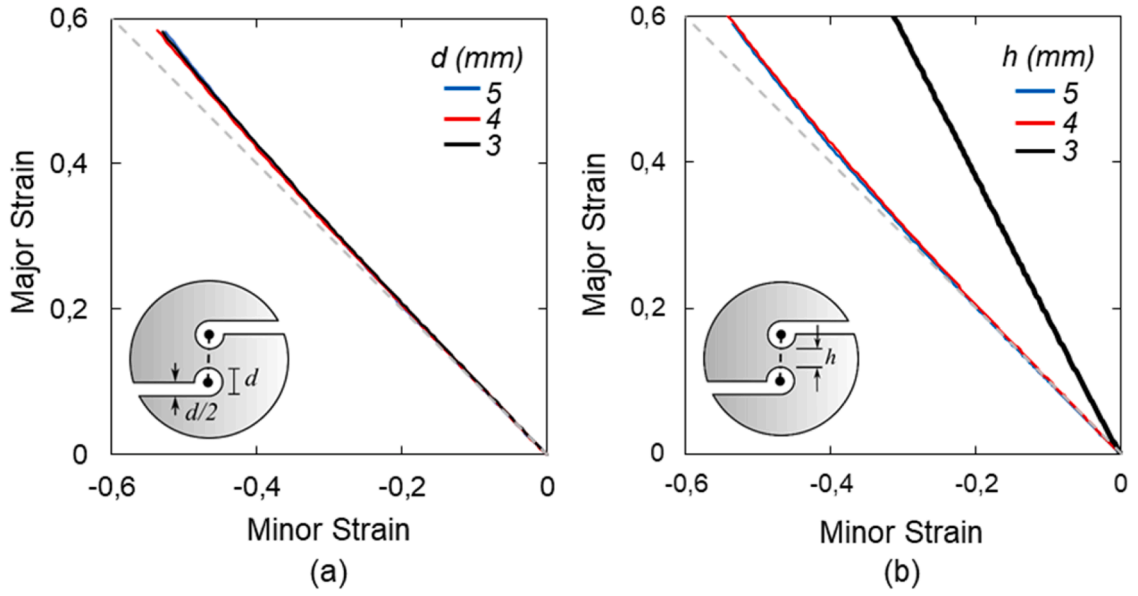

Fig. 8. Numerical analysis of the effect of (a) the hole diameter $\boldsymbol{d} = \{5,\ 4, 3\}$ ***mm*** and (b) the ligament height $\boldsymbol{h} = \{5, 4, 3\}$ ***mm*** on strain loading path.

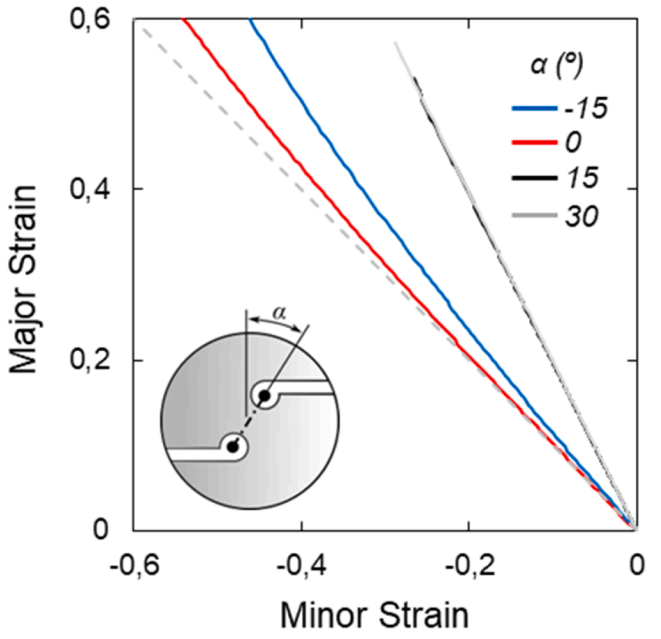

Fig. 9. Effect of the orientation angle $\boldsymbol{\alpha}$ on the strain loading path ($\boldsymbol{d} = 5$ ***mm***, $\boldsymbol{h} = 5$ ***mm***).

this research has an average external diameter of $d_0 = 38.1$ *mm* (1.5 *in*) and an average wall thickness of $t = 1.25$ *mm* (0.049 *in*) in the 'as-received' condition. The tensile specimens were machined along the axial tube direction at different angles along the circumferential direction, as depicted in Fig. 10a, whereas the dimensions of the resulting specimens are also provided in this figure.

The tensile tests were carried out at room temperature on an Instron™ SATEC 1190 Series (Model 1196) testing machine of 250 kN, following the ASTM standard [35]. The strain measurements were conducted using a 25 mm extensometer. In addition, the commercial digital image correlation (DIC) ARAMIS™ Professional 2020 system was used to obtain additional principal in-plain strain measurements. Six valid tests were performed with specimens cut at different angles along the circumferential direction. In all tests, true strain at failure was slightly below 0.2. The stress-strain curve was extrapolated, for the case of forming processes achieving higher levels of equivalent strain, by fitting the experimental stress-strain evolution and the measurements of thickness at fracture using optical microscopy, resulting in the true stress-strain curve depicted in Fig. 10b.

3.2. Shear tests on tubes

This section focuses on the experimental setups used for the novel tests proposed, i.e. STC and STT, used for the accurate assessment of the SFFL of thin-walled tubes. To this purpose, the testing equipment and experimental plan, the strain measurement and the procedure for the determination of fracture strains are presented and explained.

3.2.1. Experimental equipment

In the case of the STC test, Suzpecar MEM102 electromechanical press of 50 tonnes was utilized (see Fig. 11a). For the STT test, the universal testing machine Instron™ SATEC Model 1196, equipped with control and data analysis software for static tests SCM3000, was employed together with the experimental setup depicted in Fig. 11b. In both cases, the equipment controllers were programmed to execute the appropriate test sequences, determining the moving element approach speed, preload, test speed, fracture detection, maximum displacement, and recording force and displacement data over time. For both tests, the ARAMIS™ Professional 2020 DIC system was used for obtaining the principal in-plain strain evolutions until the onset of failure in the different testing specimens. Thus, Fig. 11 provides a detailed view and a visual explanation of the experimental tests performed for the STC and STT tests, respectively.

3.2.2. Experimental plan

The experimental plan for the two innovative testing procedures, i.e. the STC and the STT tests proposed, is presented in Table 3. This experimental plan includes 4 testing conditions for each of them, labelled with a test name, corresponding to the sets of parameters selected for the STC test in Section 2.2 and for the STT test in Section 2.3, respectively. As provided in Table 3, only geometric parameters are considered in this experimental plan: width w and height h in the case of STC (see Fig. 2a), and the alignment angle α for the STT (see Fig. 6a), are employed. In addition, with the aim of ensuring the statistical meaning of the experiments, a minimum of three replicates were conducted for each testing geometry. Finally, it must be pointed out that the different

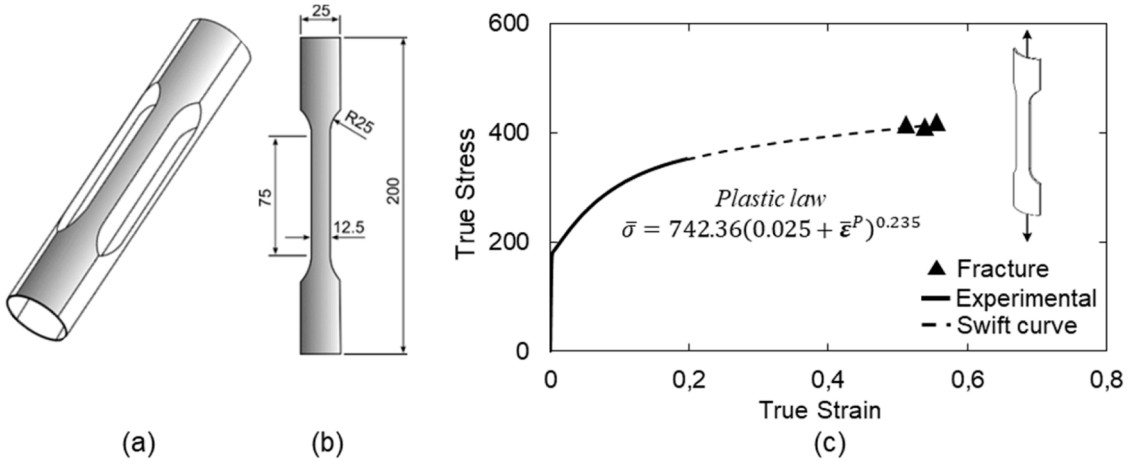

Fig. 10. (a) Tensile specimens machined from the tube at different angles, (b) dimensions of the testing specimens, and (c) stress-strain curve obtained from tensile testing.

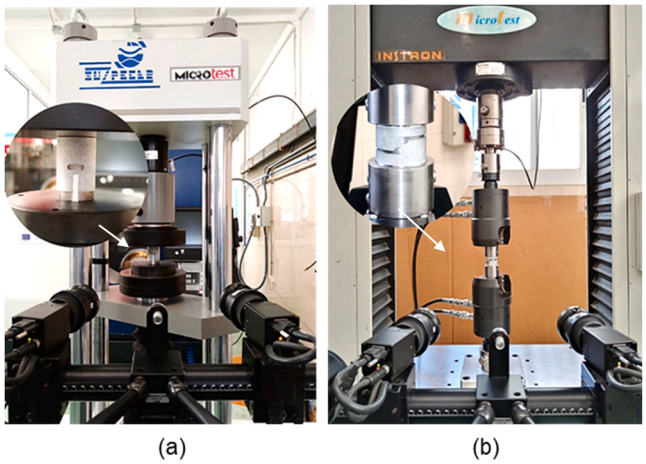

Fig. 11. Testing setup and equipment used for: (a) Shear test by compression STC and (b) Sher test by tension STC together with the DIC system ARAMIS™ Professional 2020.

Table 3
Selected values of testing parameters for STC and STT tests.

	Test	w (mm)	h (mm)
STC	C5 × 3	5	3
	C5 × 5	5	5
	C10 × 3	10	3
	C10 × 5	10	5
	Test	**h (mm)**	**α (°)**
STT	T15	4	−15
	T00	4	0
	T15	4	15
	T30	4	30

specimens were manufacturing using a variety of machine tools and conventional CNC machining operations. In the case of the STC specimens, the slots were obtained by means of side milling operations. After that, face milling was utilized to achieve the final shape of the longitudinal slot. The STT specimens were manufactured via drilling and milling in a CNC machining centre, being the grooves milled as the tube was rotating. Finally, it must be noted that all the slots, grooves and notches were polished in order to obtain good surface finishing of the corresponding geometries.

3.2.3. Strain measurement

As exposed above, the measurement of the in-plane principal strains for the STC and STT tests was conducted using the automated optical system ARAMIS™ Professional 2020 based on digital image correlation (DIC). This system consists of two cameras of 5 megapixel of resolution (2448 × 2050 pixels) set at a recording frame rate of 4 frames per second (4 Hz) within a predefined analysis area in order to reduce the processing time. In this case, the surface component required for the strain analysis was generated using a facet size of 12 pixels and a grid spacing of 6 pixels.

Initially, the analysis was performed on a larger area, as depicted in Fig. 12a, to account for the possibility of failure in other areas. However, as expected and later experimentally confirmed, the highest plastic strains occurred in the zone of the ligament. Based on this, the subsequent analysis was focused exclusively on this ligament zone, as depicted in Fig. 12b. This applies to both test specimens, i.e. STC and STT.

3.2.4. Onset of failure

In the case of both novel test designs, it is crucial to establish a criterion that provides accurately the onset of material failure. This onset of failure can be determined by different methods such as the observation of a sudden decrease in the load or a significant increase in the strain rate at a specific point near the crack, among others. In this study, the second approach is used, as far as the tests were conducted using a displacement control in the testing machines. In all the tests, cracking is observed and then the failure instant assessed when a reference point R_P, located in the lower zone of the ligament where the crack is initiated, as depicted in Fig. 13a, experiences a noticeable increase in its velocity, as shown in Fig. 13b. This increase can be also observed in a plot of the vertical displacement versus time of this reference point (Fig. 13b).

With the aim of evaluating the major strain within the crack zone at the instant of failure, three sections spaced 0.2 mm and parallel to the cracking line were analyzed, providing the point where the major principal strain had the maximum value. This strain-based failure criterion was used, as it is assumed that it provides a fair approximation of the point P_F where failure is initiated. The variation of ε_1 along the 3 parallel sections is depicted in Fig. 14. The starting point of the measurement starts at the top and finishes at the bottom of the sections, providing the location of point P_F.

3.2.5. Fracture strains

The experimental procedure for determining fracture strains involves the measurement of the tube thickness along the crack after fracture to obtain the 'gauge length' strains. This procedure is explained

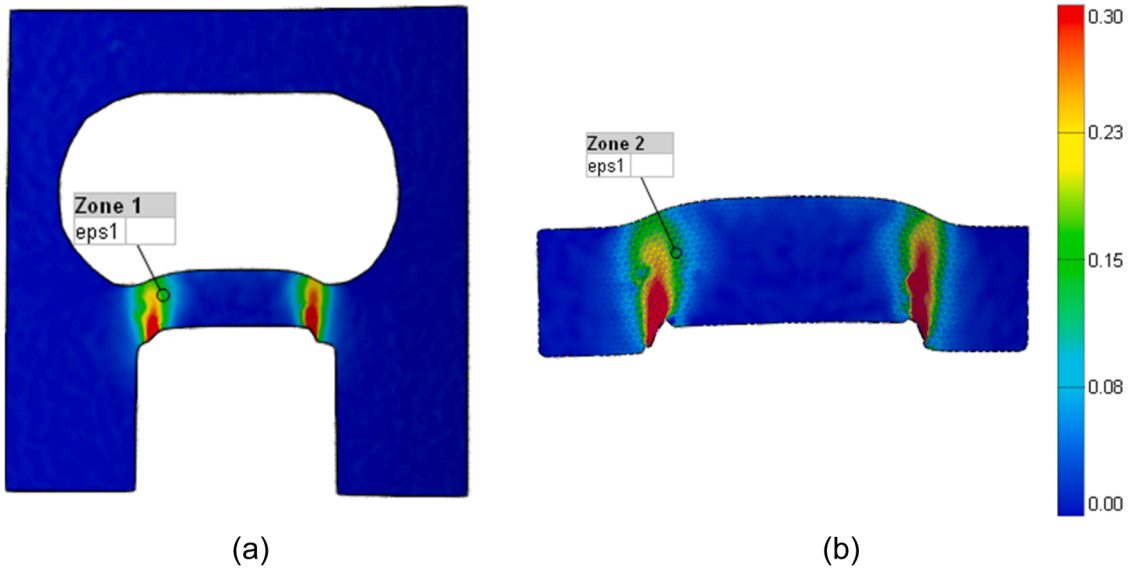

Fig. 12. Contour of major principal strain of ε_1 in the case of a STC specimen evaluated (a) at a larger surface and (b) focusing on the ligament zone.

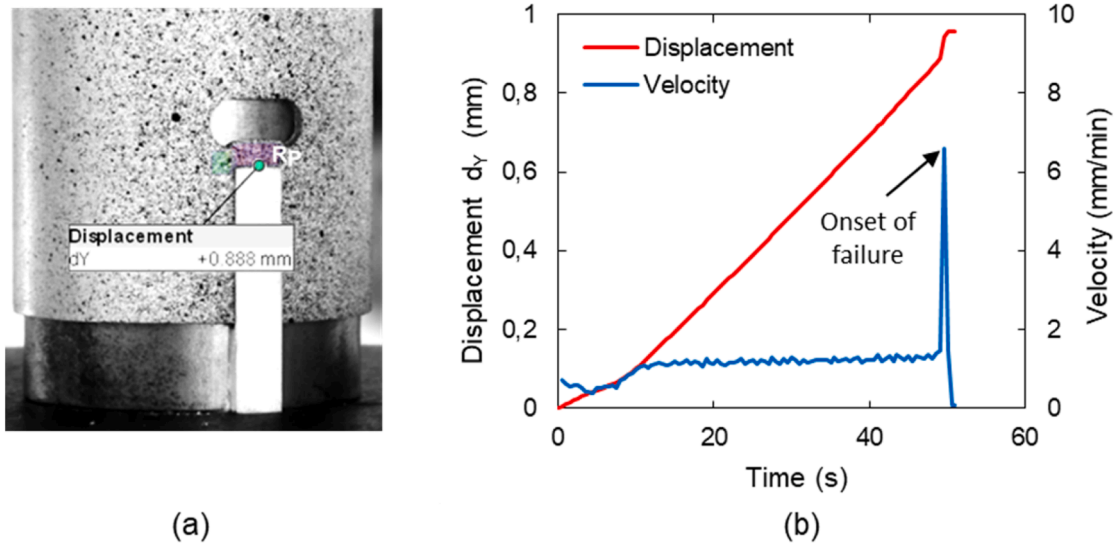

Fig. 13. (a) STC Testing specimen indicating the position of the reference point R_P used for identifying the onset of failure and (b) vertical displacement versus time of the point R_P.

in detail in reference [36], and has been intensively used by the authors both in sheet metal [37–39] and tube [27]. The measurements were performed along the crack surface using a Nikon™ SMZ800 stereomicroscope at × 15 magnification, and the data was processed using the Nikon™ NIS-Elements software. As shown in Fig. 15a, the zone of fracture initiation was evaluated, providing the thickness at fracture through the average of several values of t_f in the zone of maximum thickness reduction.

Based on the determination of the thickness at fracture, a method was established to assess the fracture strains. The method is based on extrapolating the principal strain evolution until it intersects a line corresponding to the thickness reduction at fracture, which can be calculated using the equation $\varepsilon_{3f} = \ln\left(t_f / t_0\right)$. This procedure is explained graphically in Fig. 16.

4. Results and discussion

This section presents the main results of the investigation, discussing those concerning the STC test in Section 4.1, STT in section 4.2, and providing the actual experimental assessment of the SFFL in thin-walled tube in section 4.3.

4.1. Shear test by compression

Due to the symmetry of the STC specimens, plastic deformation develops almost simultaneously at both ends of the ligament. Indeed, the crack starts at the lower edges of the vertical notch and propagates towards the upper edges. It is noteworthy that fracture does not occur simultaneously at both sides. In this regard, the fracture strains were evaluated from the side on which fracture first occurred, which was identified using the DIC system. Fig. 17a depicts, for each set of parameters, a STC specimen tested until fracture for each case, whereas Fig. 17b shows a detailed view of the failure zone of those specimens, indicating the location of the reference point R_P.

The evolution of the principal strains until fracture was then obtained by using the system ARAMIS, providing the contour of major

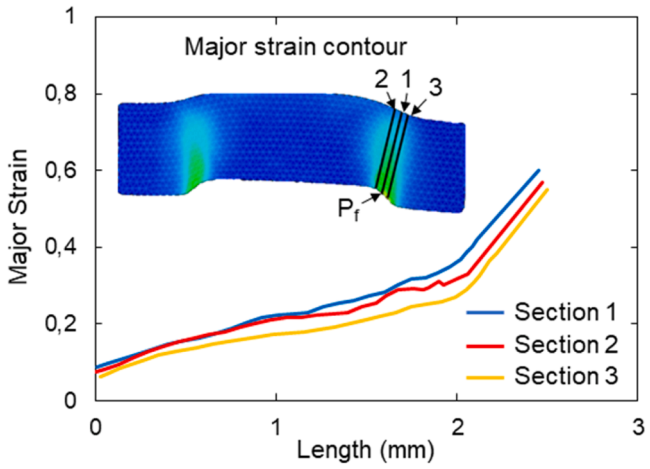

Fig. 14. Variation of ε_1 along 3 sections parallel to the cracking line.

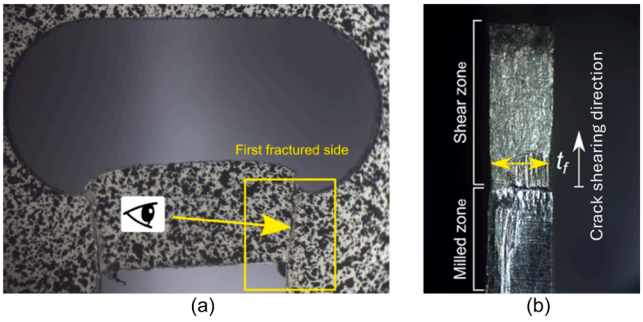

Fig. 15. Fracture strains: (a) fracture side evaluated and (b) thickness at fracture.

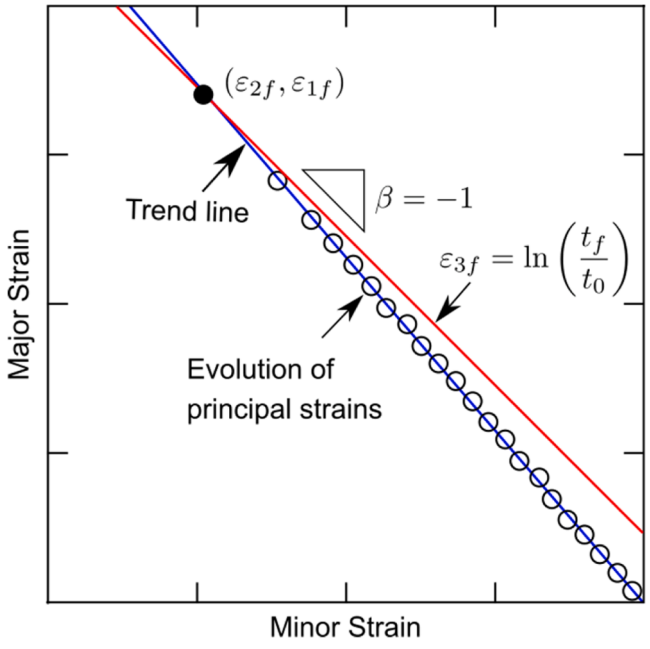

Fig. 16. Schema of the determination of the fracture in-plane principal strains using the average thickness at fracture.

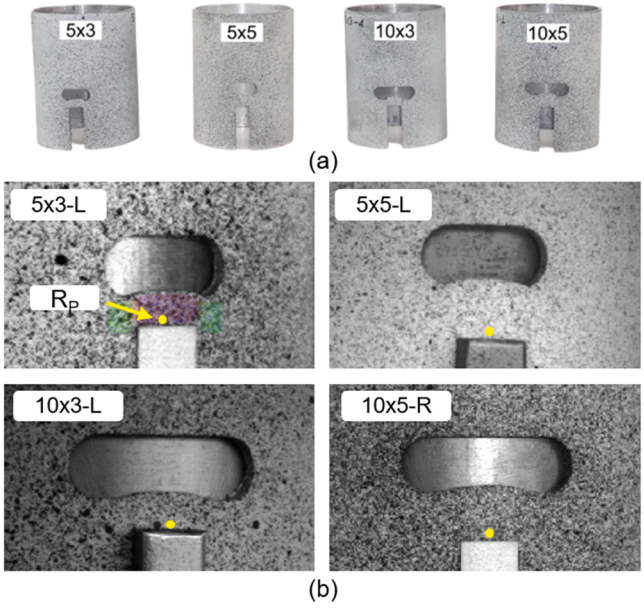

Fig. 17. Resulting specimens of the STC test: (a) Specimens tested until fracture, and (b) detailed fracture zone depicting the reference points used for the assessment of failure. The label wxh within (b) represents the width and the height of the groove, respectively, whereas L and R indicate the side at which fracture occurred.

strains ε_1 depicted in Fig. 18 for each STC test case. The processing of the in-plane principal strains along the test deformation stages allowed obtaining the point and instant at which fracture initiates for each case. To this regard, the contours of major strain shown in Fig. 18 correspond to the stage when the crack begins. In addition, those major strain contours clearly illustrate the shear effect in the lower part of the ligament, with higher major strain values observed in the corners, which is the location where fracture initiates.

Fig. 19 shows the evolution of the principal strains for each case corresponding to the STC test. The evolution represented by black circles depicts the experimental strain measurements provided by the system ARAMIS at the point where the crack initiates. The blue dashed line is the trend line obtained by linear fitting of the experimental results, whereas the black line represents the geometric locus $\varepsilon_3 = \varepsilon_{3f}$, i.e. constant thickness of fracture. The intersection point of these two lines provides the in-plain fracture strains, as explained in Section 3.2.

As can be seen in the strain evolutions depicted in Fig. 19, the fracture points for the 4 test cases analyzed are concentrated in a small region. Indeed, the major strains at fracture are within a range of $0.57 < \varepsilon_1 < 0.69$, whereas the values of the minor strain at fracture are in a range between $-0.63 < \varepsilon_2 < -0.55$. In addition, the values of the principal strain ratio are within the range $-0.94 < \beta < -0.84$, i.e. around 0.9 and close to pure shear conditions. Thus, the STC provides accurate results to assess the SFFL [34] close to $\beta < -1$, as well as for the standard shear tests [40] utilized in [41], but in this case using the specific tube geometry.

At this point, a validation of the numerical model is crucial to ensure that the combined numerical and experimental procedure provides suitable results. As typically carried out by the authors [42–44], the numerical model was validated in terms of principal strains in a section parallel to the crack at the instant of the crack initiation, using identical conditions of the selected experimental test, including the exact geometry and the displacement of the sliding die at the precise instant of failure. To this regard, Fig. 20b provides the comparison of the in-plane principal strains of the selected section (see Fig. 20a) comparing the results provided by the DIC system and the numerical model. As can be seen in Fig. 20b, the correspondence between the numerical model and

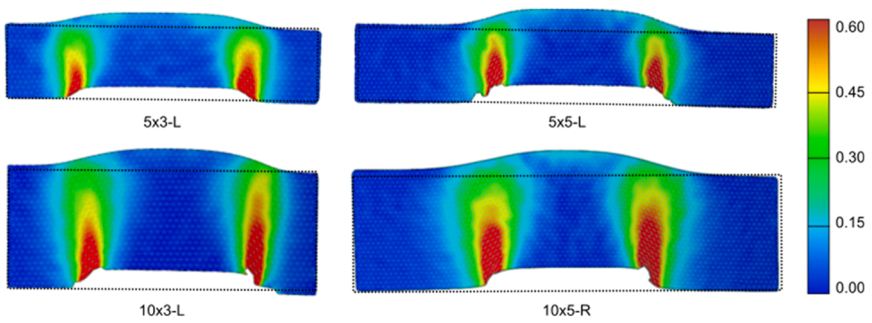

Fig. 18. Contour plot of major strain provide by DIC system for each test case.

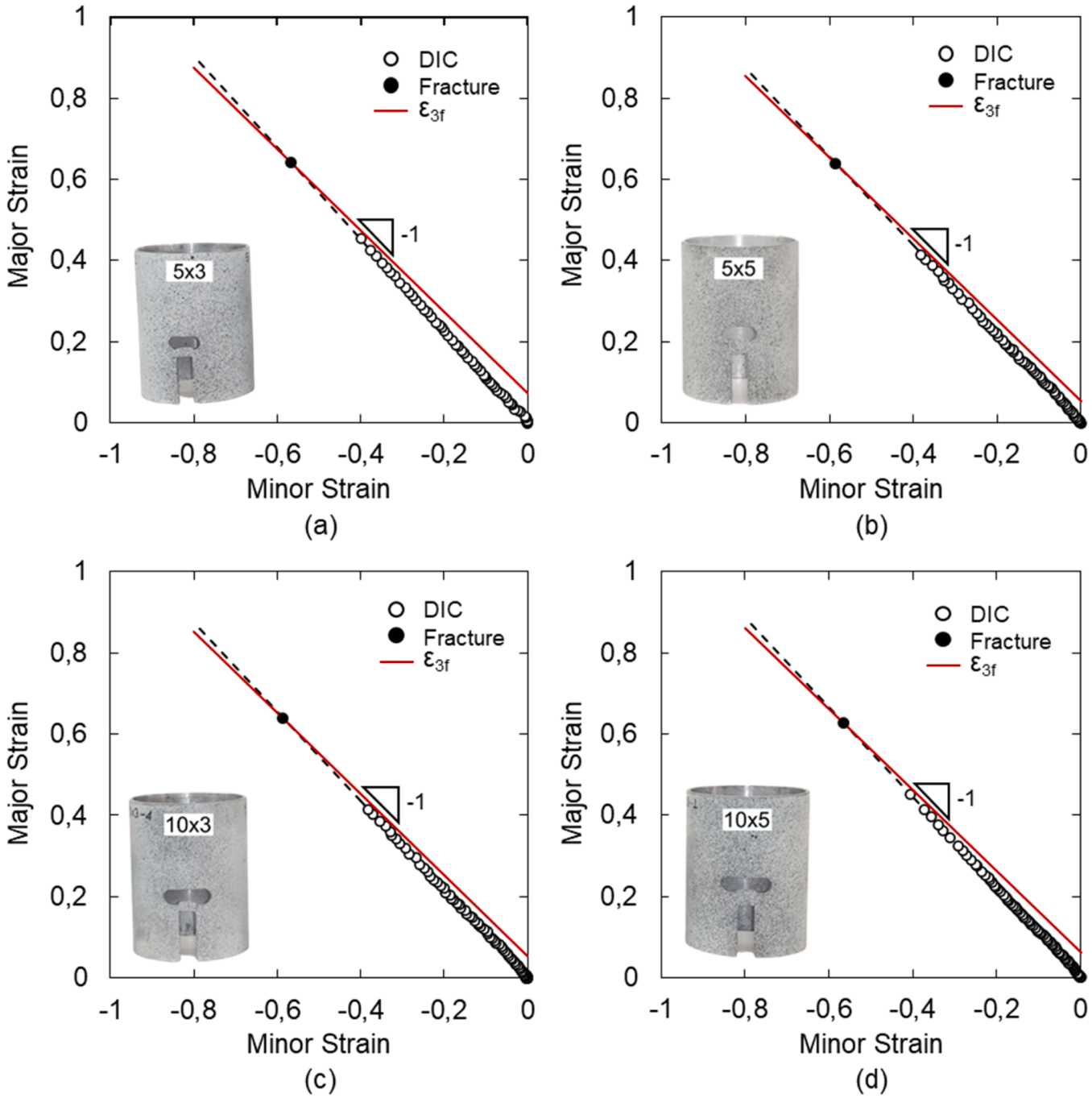

Fig. 19. Strain loading paths and fracture points for selected STC tests: (a) w = 5, h = 3, (b) w = 5; h = 3, (c) w = 10, h = 3, (d) w = 10, h = 5.

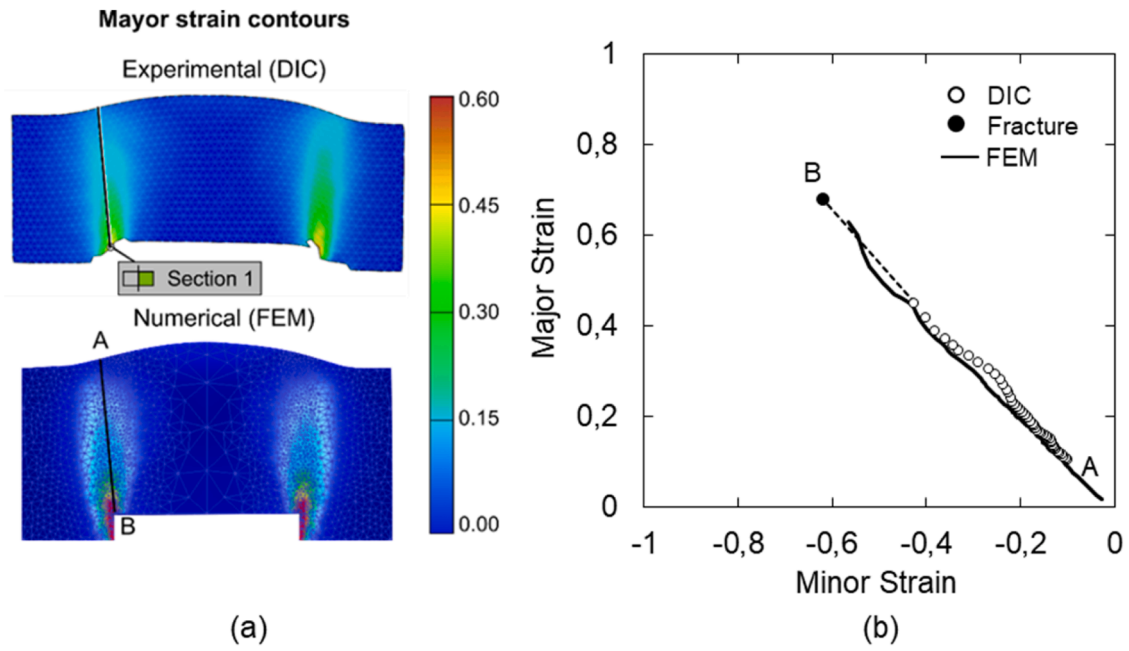

Fig. 20. Validation of numerical modelling of STC: (a) Experimental and numerical major strain contours, and (b) comparison of numerical vs. experimental strains along the selected section.

the experimental results is fairly accurate along the whole section.

Additionally, it must be pointed out that the level of principal strains provided by the DIC system are slightly below the strains provided by the numerical model, as far as the ARAMIS system cannot provide strain values at the very notch edge. This is because the experimental strains at point B (see Fig. 20, below) are smaller than those predicted by the FE model. Nevertheless, up to this level of experimental strains attained by the point B, experimental and numerical predictions are almost coincident. Finally, as can be also seen in Fig. 20b, the strain state remains close to pure shear along the entire fracture section, thereby confirming the validity of the STC for providing fracture points close to pure shear conditions.

4.2. *Shear test by tension*

In the case of the STT test, the specimen has a plane of symmetry along the length of the tube, as it has two equal ligaments, one in the frontal face (see Fig. 21a) and the other in the back. The tensile force produces fracture in the ligament zone beginning at any of the two faces, being the principal strain evolution similar in both, thus making the strain measurement reliable until the onset of failure. Fig. 21a depicts a STT specimen tested until fracture for each set of parameters. In addition, Fig. 21b depicts a detailed view of the fracture zone at the precise instant of failure for the different testing specimens, indicating the location of the reference point for an alignment angle of -15°.

Although the purpose of the test is the characterization of failure in mode II of fracture mechanics, the failure mode was found to be related to the alignment angle α. Indeed, mode II, i.e. in-plane shear, was the mode of failure for angles of 0° and 15°. On the contrary, in the case of alignment angles of -15° and 30°, i.e. outside the range $0^{\circ}-15^{\circ}$, the crack opening occurred in a mix mode between mode I and mode II induced by an excessive bending at the ligament zone. A schematic view of the failure attained in the STT tested specimens is shown in Fig. 22. To this regard, the STT test was able to provide the characterization of a zone of the SFFL from mode II towards the transition to mode I.

The distributions of the principal strains in the ligament zone provided by the DIC system ARAMIS for the STT tests with different orientation angle α are depicted in Fig. 23. For $\alpha = 0^{\circ}$ and $\alpha = -15^{\circ}$, the highest levels of the major strain were located in the central part of the ligament, indicating that failure was dominated by in-plane shear. However, for $\alpha = -15^{\circ}$ and $\alpha = 30^{\circ}$, the highest major strains were found on the upper left side of the notch, resulting in other modes of failure (mode III and mode I, respectively). Notice that the dotted shapes in Fig. 23 correspond to the undeformed initial state.

To this concern, Fig. 24 presents the evolution of the in-plane principal strains until fracture for the 4 cases of the angle α considered. The strain path is depicted using black circles corresponding to the pairs of in-plain principal strains provided by the DIC system until the onset of failure. The dashed blue lines represent the kink of the strain path until fracture, whereas the black solid lines represent the geometric locus of $\varepsilon_3 = \varepsilon_{3f}$, calculated using the thickness at fracture measured using optical microscopy. The intersection of the dashed blue line with the solid black line provides the fracture point, represented by a solid black circle.

As can be observed, the strain loading paths for $\alpha = -15^{\circ}$ (Fig. 24a) and $\alpha = 30^{\circ}$ (Fig. 24d) have a strain ratio close to a uniaxial stress state ($\beta = -1/2$), and thus they should not be reliable for the assessment of the SFFL. Although these configurations do not produce fracture in mode II, these two cases permit the establishment of a range of the alignment angle α in which the shear test is feasible. Indeed, in the cases of $\alpha = 0^{\circ}$ (Fig. 24b) and $\alpha = 15^{\circ}$ (Fig. 24c), proportional strain loading paths were obtained until almost the crack initiation. After that a localization process occurred resulting in the kink of the strain path shown, which was assessed assuming $\varepsilon_2 = \varepsilon_{2f} = \varepsilon_{min}$, i.e. estimated to be within local plane strain conditions until reaching fracture defined by $\varepsilon_3 = \varepsilon_{3f}$, corresponding to the thickness at fracture evaluated using microscopy.

In relation to the paths with $\alpha = 0^{\circ}$, a close to pure shear strain evolution is attained, while in the case of $\alpha = 15^{\circ}$, the strain path was slightly upwards deviated from pure shear. Contrary to the results of the STC test, the range of variation of the principal strain ratio is wider for the case of the STT test, varying the minor strain at fracture in the range of $-0.61 < \varepsilon_2 < -0.50$ and the major strain at fracture within a narrower range of $0.65 < \varepsilon_1 < 0.70$.

It must be also pointed out that, in the STT test plastic deformation occurs over the entire height h of the ligament, in some cases accompanied by a significant distortion within this plastic deformation area (as depicted in Fig. 23). However, in all the cases the DIC system was able to

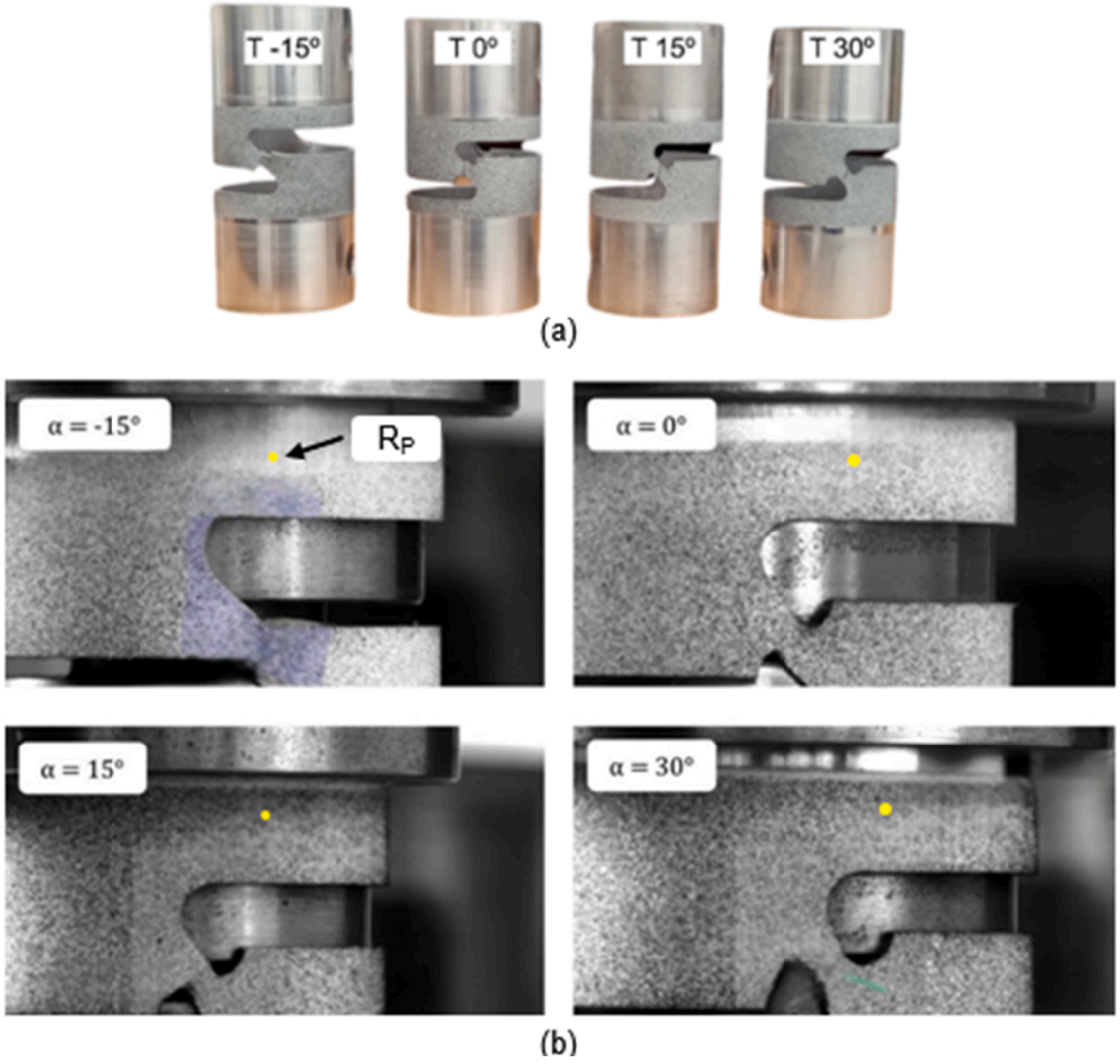

Fig. 21. STT shear test under tension: (a) Specimens until fracture, and (b) detailed fracture zone at the precise instant of failure.

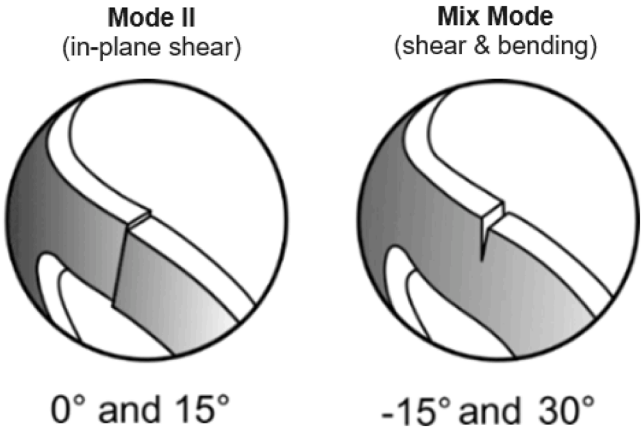

Fig. 22. Schematic view of the failure modes obtained in the STT tests depending on the angle $\boldsymbol{\alpha}$.

compute almost all facets up to a stage just prior to failure.

In addition, in the case of the STT test, the numerical results were validated using a similar procedure to the one used for STC, i.e. in terms of the principal strain field, in this case comparing numerical and experimental strains for a section parallel to the crack. To this regard,

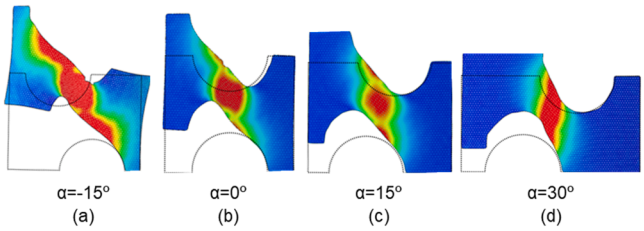

Fig. 23. Contour of the major principal strain $\boldsymbol{\varepsilon}_1$ provided by DIC system for the STT test cases. (a)$\boldsymbol{\alpha} = -15^{\circ}$, (b) $\boldsymbol{\alpha} = 0^{\circ}$, (c) $\boldsymbol{\alpha} = 15^{\circ}$ and (d) $\boldsymbol{\alpha} = 30^{\circ}$.

the results for the case of $\alpha = 0^{\circ}$ are shown in Fig. 25. These results were obtained by using the exact geometry numerically and experimentally, with the same location of the crack initiation point, and an equal displacement corresponding to the instant of failure. Fig. 25a shows the contour of principal strains in this section parallel to the crack in both cases, i.e. provided by DIC and FE, respectively, whereas Fig. 25b provides the comparison of numerical versus experimental principal strains along the selected section parallel to the crack. As can be seen, a good agreement in terms of strain distribution and the corresponding values can be observed from these results. Nevertheless, it can be noticed a certain difference in both edges of the section due to the incapacity of the DIC system to capture the strains at the notch boundaries. In any

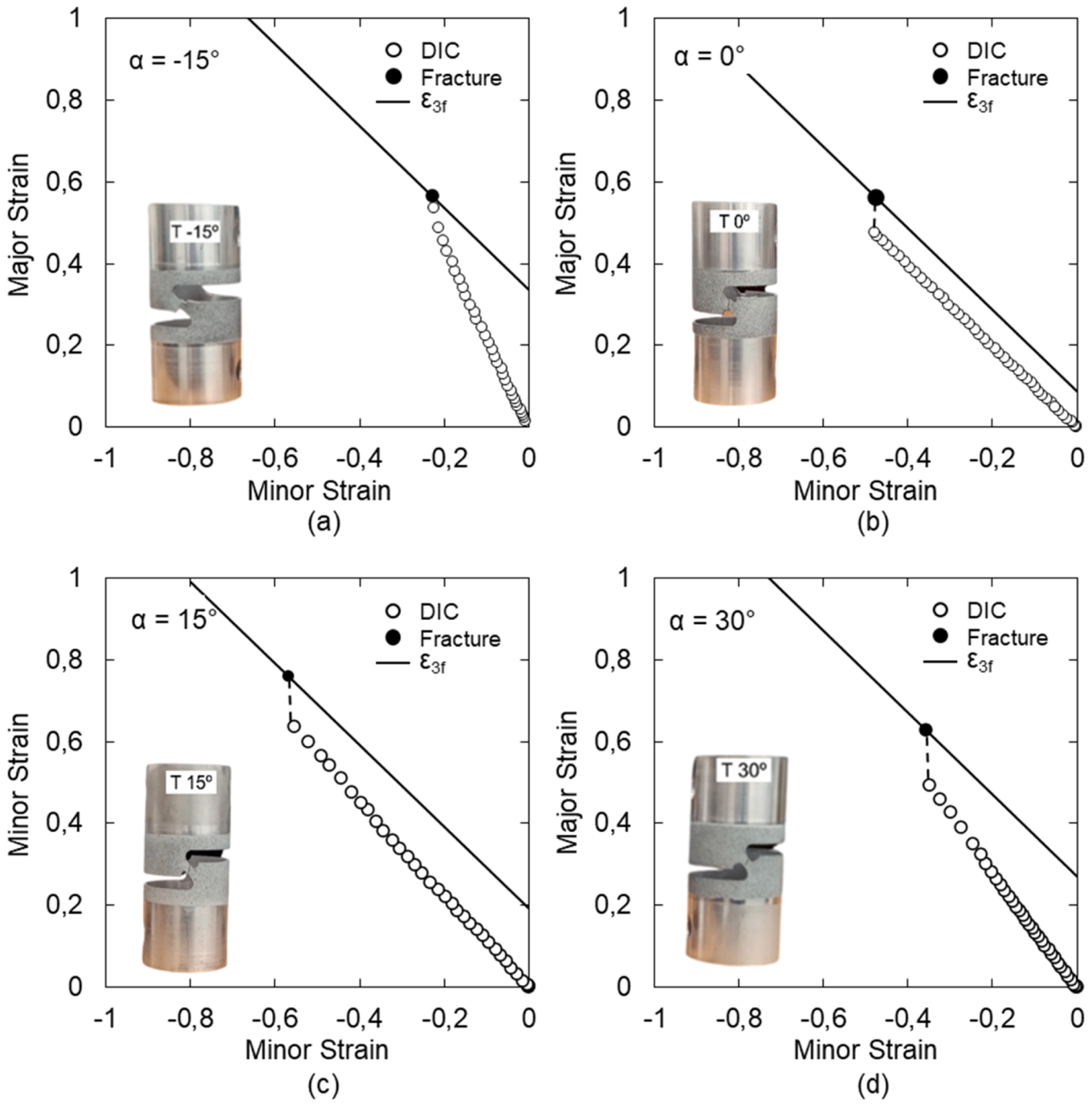

Fig. 24. Strain loading paths and fracture points for selected STT tests: (a) $\alpha = -15^{\circ}$, (b) $\alpha = 0^{\circ}$, (c) $\alpha = 15^{\circ}$, and (d) $\alpha = 30^{\circ}$.

case, the numerical model has demonstrated that it provides an accurate strain field within the whole plastic deformation area, including the values at the edges. As can be also observed, the highest level of strains is within the central zone (point B in Fig. 25a), coinciding with a principal strain ratio β close to -1 and thus confirming that fracture is produced in mode II. Point A, located at the upper edge, is also within a strain state close to pure shear, but at a lower strain level, whereas point C, located at the lower edge, is showing a certain trend towards the transition to uniaxial tension. This might be the reason of the onset of fracture in mode I produced under certain cases of α.

Finally, it must be pointed out that the validation of the numerical model, in this case for the STT test, serves also for the validation of the whole procedure presented for the determination of the SFFL. As in the case of the STC test, the validation is needed for the correct transformation of the resulting SFFL points from the principal strain space to the equivalent strain versus stress triaxiality space for non-proportional loading paths analysis, as carried out by Suntaxi et al. [30] in the case of SPIF of tubes.

4.3. Assessment of the SFFL

In previous studies, such as [33,34], the SFFL is defined theoretically as a line with a slope of 1, as the FFL is the fracture locus of mode I with a slope of -1. However, the experimental results usually provide a different slope of the FFL, as well as it happens with the SFFL obtained using the average shear fracture strains calculated for each test geometry. To this regard, Table 4 summarizes the average results (for the successful test cases and using the denomination previously presented in

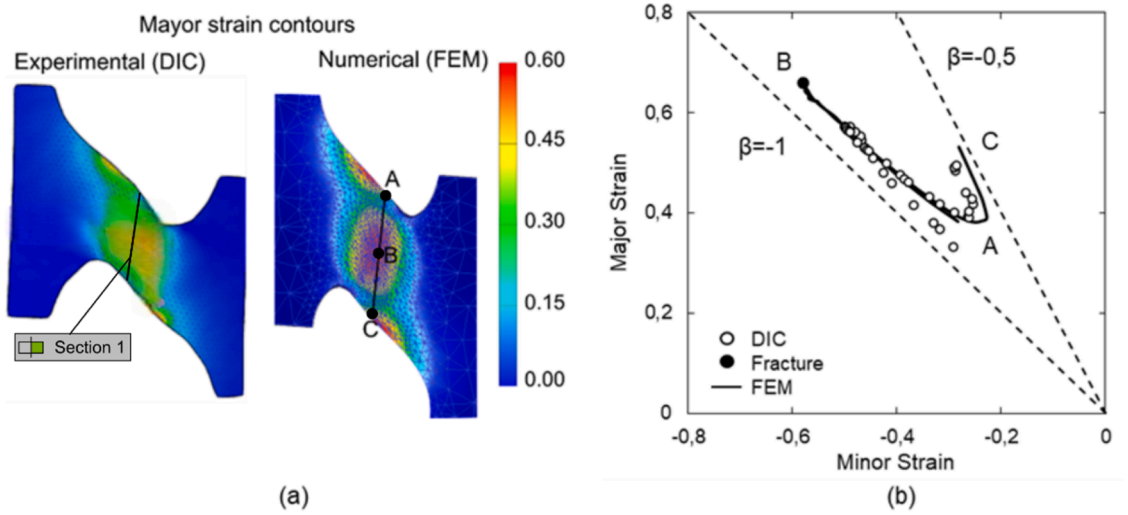

Fig. 25. Numerical and experimental results corresponding to the case of $\alpha = 0°$ along a section parallel to the crack: (a) Contour of principal strains provided experimentally by the DIC and numerically by the FE analysis, and (b) numerical versus experimental strains along the depicted section parallel to the crack.

Table 4
Average values of the principal strains at fracture in the different STC and STT tests.

Case	$\bar{\varepsilon}_{1f}$	$\bar{\varepsilon}_{2f}$	SD ($\bar{\varepsilon}_{1f}$)
C5 × 3	0.63	−0.53	0.012
C5 × 5	0.63	−0.59	0.090
C10 × 3	0.65	−0.57	0.012
C10 × 5	0.66	−0.58	0.020
T00	0.62	−0.44	0.016
T15	0.69	−0.51	0.014

Table 3) of the major and minor strains at fracture, together with their standard deviation SD of the major strain, used for constructing the SFFL.

To this regard, Fig. 26 depicts the resulting experimental SFFL together with the average fracture points presented in Table 4, also depicting the corresponding standard deviation by using a scatter band

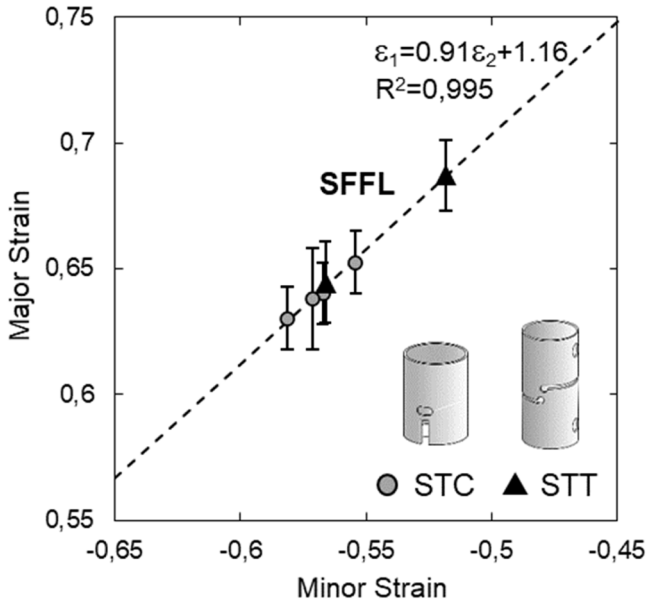

Fig. 26. Resulting experimental SFFL obtained from the STC and STT new test designs.

for each case. The linear fitting of the resultant shear fracture forming limit or SFFL for the AA6061-T4 tube studied, is finally represented by the equation $\varepsilon_1 = 0.91\varepsilon_2 + 1.1$.

In contrast to the theoretical slope of 1 of the SFFL, the experimental results for this case provided a slightly different slope of 0.91, which is not significantly different of this ideal value. This discrepancy suggests that there might be some second order failure mechanism when fracture by in-plane shear occurs beyond those assumed in [33,34]. Nevertheless, as pointed out, a SFFL slope of 0.91 is not significantly far from the theoretical one of this fracture locus.

It can be also noticed in Fig. 26 that the lower extreme point of the SFFL corresponds to the STC configuration width $w = 5\ mm$ and $h = 5\ mm$, whereas the upper extreme point corresponds to the STT configuration with an alignment angle of $\alpha = 15°$. This implies that by using only these two configurations, it would have been possible to obtain a relatively feasible SFFL. The other tests considered are not far from the lower extreme point, i.e. close to pure shear conditions. These tests provide, as can be observed in Fig. 26, a further confirmation of the validity of the SFFL obtained by the two novel test designs. In any case, the combination of all these configurations allows to assess a more reliable SFFL, as they have proven to provide consistent results.

5. Conclusions

This research work has presented two novel test designs based on the specific thin-walled tube geometry that have demonstrated experimentally to provide an accurate characterization of the fracture locus in mode II of fracture mechanics, which is represented by the shear fracture forming limit (SFFL). The combined numerical and experimental procedure has been applied to AA6061-T4 thin-wall tube, providing the SFFL by making use of 4 configurations of the test under compression or STC and 2 configurations of the tests under tension or STT.

The principal strain paths have been demonstrated to be primarily influenced by a number of geometrical parameters that are can be easily set for providing a suitable range of principal strain ratios allowing the accurate assessment of the SFFL. In this particular case, for the STC test, adjusting the width and the height provided principal strain ratios within the range −0.93 to −0.84. On the other hand, for the case of the STT test, a variation of the alignment angle between 0° and 15° allows attaining principal strain ratios up to approximately −0.7. Nevertheless, it was demonstrated that values outside the specific range could induce bending, which might result in a fracture transitioning towards Mode I of fracture mechanics.

The results obtained, and the proposed overall methodology based on a combined numerical and experimental analysis, confirmed that the SFFL can be accurately evaluated in thin-walled tubes for specimens that in the case of both tests are based on the particular tube geometry. This provides a valuable tool for characterizing the SFFL of thin-walled tubes.

Finally, the validation of the whole procedure, including the proven accuracy of the numerical model, allows performing an accurate transformation of the SFFL locus obtained into the equivalent strain versus stress triaxiality state, which has demonstrated to be a valuable framework for the analysis of non-proportional forming processes, as it is for instance the particular case of single point incremental forming of tube ends.

CRediT authorship contribution statement

C. Suntaxi: Writing – original draft, Software, Investigation, Formal analysis, Data curation, Conceptualization. **J.A. López-Fernández:** Writing – original draft, Visualization, Validation, Investigation, Data curation. **G. Centeno:** Writing – review & editing, Project administration, Methodology, Investigation, Funding acquisition, Conceptualization. **C. Vallellano:** Writing – review & editing, Project administration, Investigation, Formal analysis.

Declaration of competing interest

The authors declare that they have no known competing financial interests or personal relationships that could have appeared to influence the work reported in this paper.

Acknowledgements

The authors acknowledge the funding received through the grant of reference TED2021-131153B-C22 funded by MICIU/AEI/10.13039/501100011033 and by the European Union under NextGenerationEU/PRTR and also through the grant PID2021-125934OB-I00 financed by MCIN/AEI/10.13039/501100011033 and by ERDF "A way of making Europe" (EU).

Data availability

Data will be made available on request.

References

[1] G. Miller, Tube Forming Procces: A Comprehensive Guide, Society of Manufacturing Engineers, Dearborn, Michigan, 2003.
[2] Z.Y. Xie, Z.X. Zhao, C. Li, Bending crashworthiness of thin-walled square tubes with multi-cell and double-tube cross-sections, J. Mech. Sci. Technol. 35 (2021), https://doi.org/10.1007/s12206-021-1001-6.
[3] L.B. Davis, M. McElroy, S. Afshan, M. Evangelista, A. Kwan, Proof Testing Aluminum and Titanium Thin-Walled Tubes for Aerospace Applications, AIAA Science and Technology Forum and Exposition, AIAA SciTech Forum 2022, 2022, https://doi.org/10.2514/6.2022-2285.
[4] F. Ma, Y. Zhao, G. Wang, Wu Liang, Y. Pu, Crashworthiness optimization design of thin-walled tube filled with re-entrant Triangles Honeycombs, Automot. Innov. 2 (2019) 1–13, https://doi.org/10.1007/s42154-019-00051-7.
[5] W.J. Joost, Reducing vehicle weight and improving U.S. energy efficiency using integrated computational materials engineering, JOM 64 (2012) 1032–1038, https://doi.org/10.1007/s11837-012-0424-z.
[6] K.B. Le, V. Van Cao, H.X. Cao, Circular Concrete Filled Thin-Walled Steel Tubes Under Pure torsion: Experiments, 164, Thin-Walled Structures, 2021 107874, https://doi.org/10.1016/J.TWS.2021.107874.
[7] T. Xu, S. Zhang, J. Liu, X. Wang, Design method of concrete filled thin-walled steel tube column-foundation connections, (2021). https://doi.org/10.1016/j.engstruct.2021.113033.
[8] F. Wang, F. Liu, H. Yang, H. Sheng, Axial compressive performances of thin-walled steel tube confined steel-reinforced concrete columns after fire exposure, Thin-Wall. Struct. 190 (2023) 110919, https://doi.org/10.1016/J.TWS.2023.110919.
[9] S.P. Keeler, Circular grid system - a valuable aid for evaluating sheet metal formability. SAE Technical Papers, SAE International, 1968, https://doi.org/10.4271/680092.
[10] G.M. Goodwin, Application of strain analysis to sheet metal forming problems in the press shop. SAE Technical Papers, SAE International, 1968, https://doi.org/10.4271/680093.
[11] J.D. Embury, J.L. Duncan, Formability maps, Annual Rev. Mater. Sci. 11 (1981) 505–521, https://doi.org/10.1146/annurev.ms.11.080181.002445.
[12] A.G. Atkins, Fracture in forming, J. Mater. Process. Technol. 56 (1996) 609–618, https://doi.org/10.1016/0924-0136(95)01875-1.
[13] F.A. McClintock, A criterion for ductile fracture by the growth of holes, J. Appl. Mech. 35 (1968) 363–371.
[14] K. Isik, M.B. Silva, A.E. Tekkaya, P.A.F. Martins, Formability limits by fracture in sheet metal forming, J. Mater. Process. Technol. 214 (2014) 1557–1565, https://doi.org/10.1016/j.jmatprotec.2014.02.026.
[15] G. Centeno, A.J. Martínez-Donaire, D. Morales-Palma, C. Vallellano, M.B. Silva, P. A.F. Martins, Novel experimental techniques for the determination of the forming limits at necking and fracture, Mater. Forming Machining: Res. Develop. 2 (2015) 1–24, https://doi.org/10.1016/B978-0-85709-483-4.00001-6.
[16] P.A.F. Martins, N. Bay, A.E. Tekkaya, A.G. Atkins, Characterization of fracture loci in metal forming, Int. J. Mech. Sci. 83 (2014), https://doi.org/10.1016/j.ijmecsci.2014.04.003.
[17] B.V. Mai, G.J. Hancock, G.D. Nguyen, C.H. Pham, Shear yielding and failure of cold-reduced G450 sheet steel, J. Constr. Steel. Res. 185 (2021) 106844, https://doi.org/10.1016/J.JCSR.2021.106844.
[18] B.V. Mai, G.D. Nguyen, G.J. Hancock, C.H. Pham, A combined theoretical-experimental approach for modelling ductile fracture of cold-reduced G450 steel sheet, Int. J. Solids. Struct. 200–201 (2020) 242–265, https://doi.org/10.1016/J.IJSOLSTR.2020.03.028.
[19] S.D. Liu, D. Meuleman, K. Thompson, Analytical and Experimental Examination of Tubular Hydroforming Limits, SAE Technical Papers, 1998, https://doi.org/10.4271/980449.
[20] X. Chen, Z. Yu, B. Hou, S. Li, Z. Lin, A theoretical and experimental study on forming limit diagram for a seamed tube hydroforming, J. Mater. Process. Technol. 211 (2011) 2012–2021, https://doi.org/10.1016/J.JMATPROTEC.2011.06.023.
[21] S. Li, X. Chen, Q. Kong, Z. Yu, Z. Lin, Study on formability of tube hydroforming through elliptical die inserts, J. Mater. Process. Technol. 212 (2012) 1916–1924, https://doi.org/10.1016/J.JMATPROTEC.2012.04.016.
[22] R. Davies, G. Grant, D. Herling, M. Smith, B. Evert, S. Nykerk, J. Shoup, Formability investigation of aluminum extrusions under hydroforming conditions, SAE Tech. Papers (2000), https://doi.org/10.4271/2000-01-2675.
[23] W.J. Song, S.C. Heo, T.W. Ku, J. Kim, B.S. Kang, Evaluation of effect of flow stress characteristics of tubular material on forming limit in tube hydroforming process, Int. J. Mach. Tools. Manuf. 50 (2010) 753–764, https://doi.org/10.1016/J.IJMACHTOOLS.2010.05.010.
[24] G. Centeno, M.B. Silva, L.M. Alves, C. Vallellano, P.A.F. Martins, Towards the characterization of fracture in thin-walled tube forming, Int. J. Mech. Sci. 119 (2016) 12–22, https://doi.org/10.1016/j.ijmecsci.2016.10.001.
[25] V.A. Cristino, J.P. Magrinho, G. Centeno, M.B. Silva, P.A. Martins, A digital image correlation based methodology to characterize formability in tube forming, J. Strain. Anal. Eng. Des. (2019), https://doi.org/10.1177/0309324718823629.
[26] J.P. Magrinho, M.B. Silva, G. Centeno, F. Moedas, C. Vallellano, P.A.F. Martins, On the determination of forming limits in thin-walled tubes, Int. J. Mech. Sci. 155 (2019), https://doi.org/10.1016/j.ijmecsci.2019.03.020.
[27] J.P. Magrinho, G. Centeno, M.B. Silva, C. Vallellano, P.A.F. Martins, On the formability limits of thin-walled tube inversion using different die fillet radii, Thin-Wall. Struct. 144 (2019), https://doi.org/10.1016/j.tws.2019.106328.
[28] V.A. Cristino, J.P. Magrinho, G. Centeno, M.B. Silva, P.A.F. Martins, Theory of single point incremental forming of tubes, J. Mater. Process. Technol. 287 (2021), https://doi.org/10.1016/j.jmatprotec.2020.116659.
[29] A.J. Martínez-Donaire, M. Borrego, D. Morales-Palma, G. Centeno, C. Vallellano, Analysis of the influence of stress triaxiality on formability of hole-flanging by single-stage SPIF, Int. J. Mech. Sci. 151 (2019) 76–84, https://doi.org/10.1016/j.ijmecsci.2018.11.006.
[30] C. Suntaxi, G. Centeno, M.B. Silva, C. Vallellano, P.A.F. Martins, Tube expansion by single point incremental forming: an experimental and numerical investigation, Metals. (Basel) 11 (2021) 1–18, https://doi.org/10.3390/met11091481.
[31] J.P. Magrinho, M.B. Silva, P.A.F. Martins, On the characterization of fracture loci in thin-walled tube forming, minerals, Metals. Mater. Series (2021) 113–125, https://doi.org/10.1007/978-3-030-75381-8_9/FIGURES/8.
[32] D.R. Shouler, J.M. Allwood, Design and use of a novel sample design for formability testing in pure shear, J. Mater. Process. Technol. 210 (2010) 1304–1313, https://doi.org/10.1016/j.jmatprotec.2010.03.019.
[33] I. Kerim, M.B. Silva, A.G. Atkins, A.E. Tekkaya, P.A.F. Martins, A new test for determining fracture toughness in plane stress in mode II, J. Strain Anal. Eng. Design 50 (2015) 221–231, https://doi.org/10.1177/0309324715576429/FORMAT/EPUB.
[34] M.B. Silva, K. Isik, A.E. Tekkaya, A.G. Atkins, P.A.F. Martins, Fracture toughness and failure limits in sheet metal forming, J. Mater. Process. Technol. 234 (2016), https://doi.org/10.1016/j.jmatprotec.2016.03.029.
[35] ASTM E8/E8M-22, Standard test methods for tension testing of metallic materials, (2022).
[36] G. Centeno, A.J. Martínez-Donaire, D. Morales-Palma, C. Vallellano, M.B. Silva, P. A.F. Martins, Novel experimental techniques for the determination of the forming limits at necking and fracture, Mater. Forming Machining: Res. Develop. 2 (2015) 1–24, https://doi.org/10.1016/B978-0-85709-483-4.00001-6.
[37] G. Centeno, I. Bagudanch, A.J. Martínez-Donaire, M.L. García-Romeu, C. Vallellano, Critical analysis of necking and fracture limit strains and forming

forces in single-point incremental forming, Mater. Des. 63 (2014), https://doi.org/10.1016/j.matdes.2014.05.066.
[38] J.A. López-Fernández, G. Centeno, A.J. Martínez-Donaire, D. Morales-Palma, C. Vallellano, Stretch-flanging of AA2024-T3 sheet by single-stage SPIF, Thin-Wall. Struct. 160 (2021), https://doi.org/10.1016/j.tws.2020.107338.
[39] J.A. López-Fernández, M. Borrego, G. Centeno, C. Vallellano, Fracture in stretch flanging by single point incremental forming, Int. J. Mech. Sci. (2024) 109438, https://doi.org/10.1016/J.IJMECSCI.2024.109438.
[40] ASTM B831-19, Standard test method for shear testing of thin aluminium alloy products, (2014).
[41] J.P. Magrinho, M.B. Silva, P.A.F. Martins, On the characterization of fracture loci in thin-walled tube forming. Forming the Future. The Minerals, Metals & Materials Series, Springer, Cham, 2021, pp. 113–125, https://doi.org/10.1007/978-3-030-75381-8_9.
[42] J.A. López-Fernández, G. Centeno, A.J. Martínez-Donaire, D. Morales-Palma, C. Vallellano, Stretch-flanging of AA2024-T3 sheet by single-stage SPIF, Thin-Wall. Struct. 160 (2021), https://doi.org/10.1016/j.tws.2020.107338.
[43] J.A. López-Fernández, M. Borrego, G. Centeno, C. Vallellano, Fracture in stretch flanging by single point incremental forming, Int. J. Mech. Sci. 278 (2024) 109438, https://doi.org/10.1016/J.IJMECSCI.2024.109438.
[44] J.A. López-Fernández, M. Borrego, G. Centeno, C. Vallellano, Fracture in stretch flanging by single point incremental forming, Int. J. Mech. Sci. (2024) 109438, https://doi.org/10.1016/J.IJMECSCI.2024.109438.